Overview of a Comprehensive MD530F Acoustic Flight Test

James H. Stephenson
U.S. Army Combat Capabilities Development Command
Aviation & Missile Center Hampton, VA, USA

Kyle A. Pascioni Mary L. Houston Colin M. Stutz
NASA Langley Research Center Hampton, VA, USA

Preston B. Martin
U.S. Army Combat Capabilities Development Command
Aviation & Missile Center Hampton, VA, USA

ABSTRACT

A cooperative flight test campaign between the US Army and NASA was performed. This test sought to characterize the acoustic emissions of a fully instrumented MD530F helicopter using a snapshot array and a phased array of microphones. The snapshot array of microphones aimed to provide even coverage across the surface of a hemisphere, providing an acoustic emission hemisphere in a single 'snapshot' of time. The phased array of microphones was designed to provide enough resolution to determine noise sources from each individual blade as well as perform source separation from main rotor and tail rotor emissions. Test conditions for the characterization effort were chosen using a traditional one-factor-at-a-time approach as well as three design of experiment approaches. Characterization conditions included constant speed level flight, descent, and ascent conditions. Transient maneuver conditions were also captured over the snapshot array. The vehicle instrumentation included measurements of pilot controls, optical sensors to measure blade azimuth locations, pitch link loads, along with strain gauges to measure structural loads blades and fuselage. This report will provide an overview of the test, document the data acquired, and provide some initial results.

INTRODUCTION

Acoustic emissions of air vehicles are a primary concern as community noise impacts can limit operations, and potentially result in areas of land incompatible with residential or commercial use (Refs. 1–3). In order to mitigate acoustic impacts from rotorcraft vehicles, it is imperative to characterize vehicle acoustic emissions with exceptional fidelity to support community noise modeling and prediction validation efforts.

To address this need, the DEVCOM Aviation & Missile Center (AvMC) and the NASA Langley Research Center (LaRC) collaborated to conduct a comprehensive acoustic research flight test using an MD530F vehicle. The collaboration aimed to develop the tools and techniques necessary to accurately and cost effectively characterize FVL, UAS, and eVTOL vehicles, where repeatability of flight test conditions might be difficult and where interactional aerodynamic noise sources may be more prevalent. These are specific concerns with future rotorcraft under development to support Army and Urban Air Mobility applications, and this experiment provides foundational work for future excellence. The experiment was conducted over a three-week period, during which 21 hours of flight testing were conducted. There were multiple objectives for this flight test, and several new pieces of equipment were deployed.

The flight test was focused on four primary objectives. First, a new snapshot array was developed to characterize vehicles in-flight for a single 'instant' in time. The snapshot array is able to produce a full hemisphere of data for future modeling efforts from a single set of half-second spectra, and is an evolution of a previously developed array from Ref. 4. The development of the snaphot array and complete analysis of its capabilities can be found in Ref. 5. The second objective was to employ a phased array to investigate the feasibility of separation and localization of broadband noise sources, as well as evaluate the effects of interactional aerodynamic noise sources (rotor-rotor, rotor-airframe, etc). The phased array design and evaluation is investigated more completely in Ref. 6. The third objective of the flight test was to evaluate the effectiveness of a design of experiments (DOE) approach to rotorcraft acoustic flight testing. This approach should reduce the amount of flight test time necessary to fully characterize a vehicle while maintaining modeling accuracy. The DOE approach and evaluation is investigated more completely in Ref. 7. The fourth and final primary objective of this flight test was to evaluate the ability of the snapshot array to capture transient maneuvering noise of a vehicle in flight. The MD530 pilot executed several aggressive maneuvers, which

The Vertical Flight Society's 81st Annual Forum and Technology Display, Virginia Beach, VA, May 20-22, 2025.

are investigated more completely in Ref. 8. This paper focuses on documenting the overall test, the conditions flown, the data acquired, and on providing samples of data the various instruments available for further analysis. This flight test was a comprehensive measurement campaign with extensive collection of synchronized on-board and ground-based data that should prove invaluable for future research and modeling efforts.

FLIGHT TEST DESCRIPTION

An MD530F (also known as MD369FF) helicopter, tail number N20AT, was used for this experiment (Refs. 9, 10). The vehicle, shown in Figure 1, is a light-utility civilian vehicle

Figure 1: MD530 vehicle landed near phased array microphones.

with a single 350 HP, turbo-shaft, Rolls-Royce 250-C30 engine. Additional aircraft rotor characteristics are shown in Table 1 and are extracted from Ref. 11. Information on the horizontal and vertical stabilizers can be found in Ref. 11, along with a comprehensive coverage of the MD530F vehicle, its capabilities, handling, and build.

This vehicle was operated in an experimental configuration with numerous on-board data systems, which will be described presently. The aircraft positional and inertial state data, described in Table 2, were measured with NASA's Aircraft Navigation and Tracking System (ANTS), which has been previously described in Refs. 12 and 4. All measured variables have been converted to the coordinate system used for this test, which is described below.

This vehicle was also outfitted with a significant suite of on-board instrumentation. A secondary single antenna GPS and inertial navigation system were used and the processed data contains the same variables as described in Table 2, but also includes a yaw measurement in degrees.

Further instrumentation included measuring pilot vehicle stick positions, rotor shaft torque, rotor rotation rate and blade azimuth position, hub link loads, and measuring various bending and torsion moments around the vehicle's fuselage and tail surfaces. A list of the on-board measurements is provided in Table 3. All data measured during this test are synchronized to Coordinated Universal Time (UTC).

GROUND INSTRUMENTATION

The ground instrumentation described is part of NASA's Mobile Acoustics Facility (MAF), operated by the NASA/Army Comprehensive Rotorcraft Acoustics Flight Test Team (CRAFTT). The MAF is a semitrailer outfitted with two quiet diesel generators, up to five 40-foot masts for mounting antennas, and can be trucked to any location within the continental United States. The MAF is used to transport all ground equipment to the flight test and serves as the command and control station during testing. The MAF is also used to maintain, store, and charge any equipment needed.

The location of all ground-based instrumentation can be seen in Figure 2 superimposed on a satellite image of the flight test location. Details of the instrumentation are described below. The flight track heading for this test was nominally 9° True, although the phased array had passes at 189° True, as well.

Microphone Instrumentation

This experiment had two primary microphone arrays (a snapshot and a phased array). The snapshot array was comprised entirely of the second generation Wireless Acoustic Measurement Systems (WAMS II), while the phased array was augmented with an additional data acquisition system. The snapshot microphone array was used for source noise characterization and developing a design of experiments approach to acoustics flight testing. The phased array was used to evaluate the capability of determining relevant contributions of individual broadband noise sources for full-scale rotorcraft in-flight.

The primary data acquisition system is WAMS II, seen in Figure 3, a remotely controlled system with local data storage. Each WAMS II unit consists of a microphone, ground board, radio antenna, GPS receiver, and on-board SD card for data storage. The standard WAMS II setup for this test consisted of a GRAS 67AX microphone embedded in a 400 mm diameter circular ground board with rounded edges. However, a secondary configuration was also used where a B&K 4964 microphone was inverted 6.35 mm above a 381 mm diameter ground board. In both of these configurations, microphones are offset from the center of the ground board to minimize the influence of edge diffraction effects, per SAE Aerospace Recommended Practice ARP4055 (Ref. 13). WAMS II microphones are sampled simultaneously and uninterrupted throughout a run at 50 kHz with 24-bit resolution.

The phased array's secondary data acquisition system used a NI PXIe-1085 chassis with three NI PXIe-4499 data acquisition cards, each with 16 channels controlled via a local desktop. This system sampled 46 Knowles microphones, used previously in other NASA flight tests (Ref. 14), that were wired directly to the chassis and sampled simultaneously and uninterrupted throughout a run at 50 kHz with 24-bit resolution. GPS timing was acquired using a NI PXI-6683H card with associated antenna.

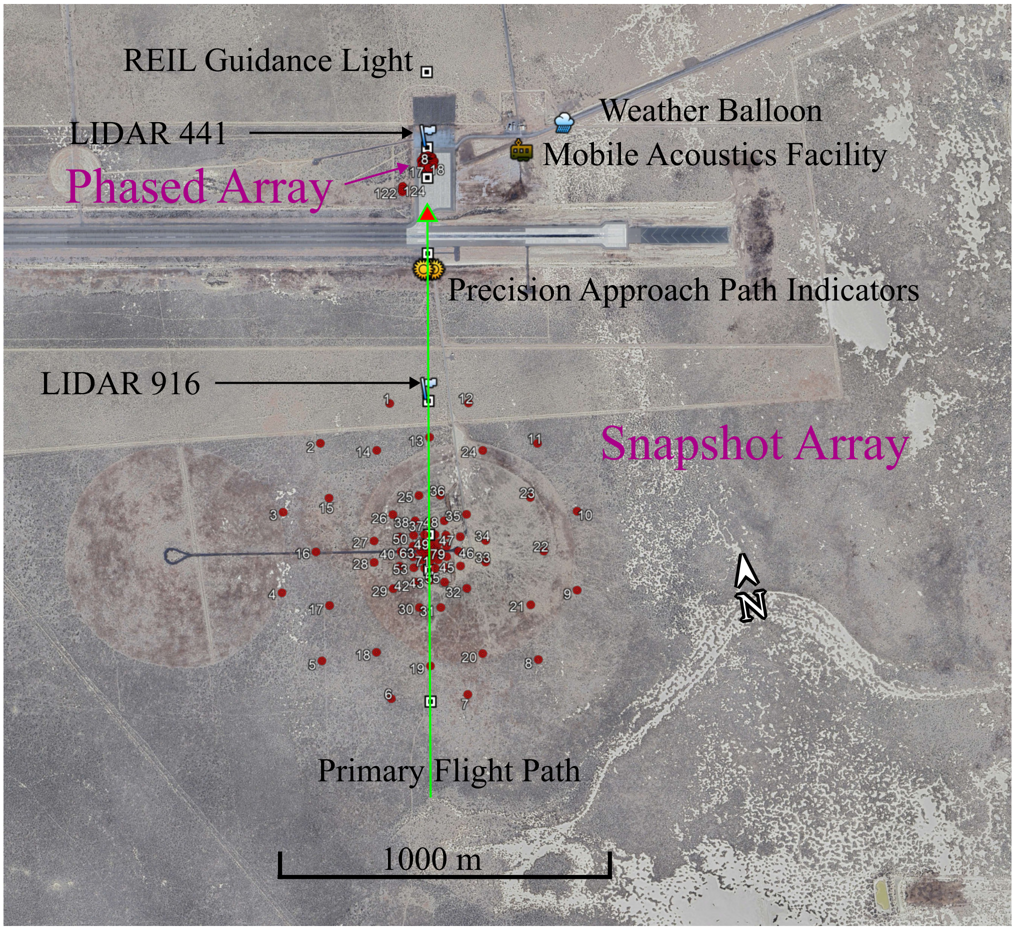

Figure 2: Location of all ground-based equipment during flight testing.

The test location was incredibly flat, as it was a former lake bed. The altitude difference measured by differential GPS between the lowest microphone and the highest microphone for all arrays was 2.65 m. This is exceptionally flat considering the microphones are spread over 1.15 sq. km (285 acres) of land. It is important to note that due to limited microphone and data acquisition capability, only one microphone array (snapshot array or phased array) was deployed on any given test day.

Snapshot Array The snapshot array was designed to create hemispheres of acoustic data sufficient for land-use planning models such as the Advanced Acoustic Model and Rotorcraft Noise Model (Ref. 15). The snapshot array consists of 79 WAMS II microphones dispersed in a manner to provide significant and almost uniform coverage of a hemisphere as the vehicle passes over the center of the array. Microphone positions were chosen using a modified 8$^{\text{th}}$ order Lebedev distribution (Ref. 16). This was convenient as a lower (4$^{\text{th}}$) order distribution is simultaneously represented, allowing for investigation to determine necessary coverage for a hemisphere in the future. 12 additional microphones were deployed near the horizon plane of the vehicle and six additional microphones were deployed directly underneath the vehicle to help mitigate slew rate challenges.

The designed hemisphere coverage for a vehicle passing over the center of the snapshot array at an altitude of 61 meters (200 feet) is shown in Figure 4. The figure shows the microphone locations on a Lambert projection as a function of azimuth (counterclockwise around the center) and elevation (radially inward). Azimuth rotates with the direction of the MD530F's main rotor as viewed from above, where 0° is the tail, 90° is the right side of the vehicle, and so forth. Elevation starts at the horizon plane (0°) and decreases radially inward, such that -90° is directly beneath the vehicle. Microphones for the snapshot array were generally numbered sequentially counterclockwise and radially from the farthest out to the innermost microphones. Microphones 1-75 were GRAS 67AX and 76-79 were inverted B&K 4964 microphones.

A Cartesian coordinate system is used, centered on microphone 79 during snapshot array days (X = Y = Z = 0). X is defined along the flight track and is positive in the primary flight direction; Y is defined perpendicular to the flight track

Figure 3: Example WAMS II deployment with GRAS 67AX microphone, data acquisition box, and tripod for antenna.

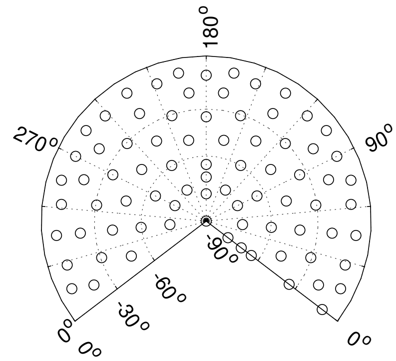

Figure 4: Hemisphere coverage of snapshot array using a Lambert projection.

and is positive to the aircraft port (left) side; Z is positive up. The microphone positions shown on the ground in Cartesian coordinates are provided in Figure 5. Significantly more details and analysis for this array are provided in Ref. 5.

The list of microphone numbers, their local ground locations, and their ideal azimuth and elevation angles are provided in Table 4.

Phased Array Generally speaking, the sources of deterministic noise (e.g., lower harmonic noise) are known and are easily distinguishable as they correspond to the blade passage frequencies of the main or tail rotor. Nondeterministic, and more specifically, broadband noise, cannot be easily identified from single-microphone measurements as being produced by the main rotor, tail rotor, or the interaction between them. Given the expected importance that nondeterministic sources may have for future FVL and eVTOL aircraft, a phased array was deployed to assess its ability to separate acoustic information amongst rotor blades.

The first phased array deployed consisted of 117 microphones in a nested pattern, and is shown in Figure 6. This array was deployed on day 201 of the year, and is referred to by that designation. Unfortunately, at the end of the first day of flights over the phased array, it appeared that the acoustic data had

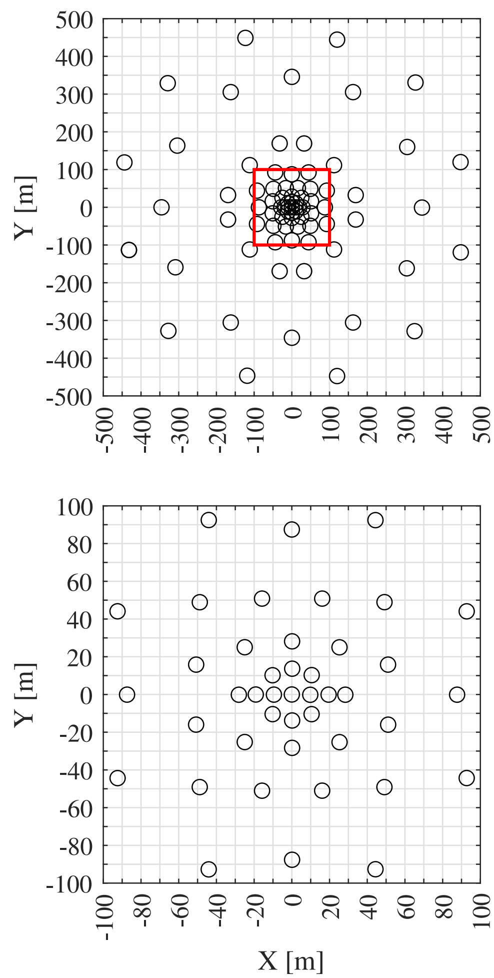

Figure 5: Snapshot array shown in local coordinate system. Top shows entire array with a red rectangle indicating the extents of the bottom figure, which shows the inner portion of the array more clearly.

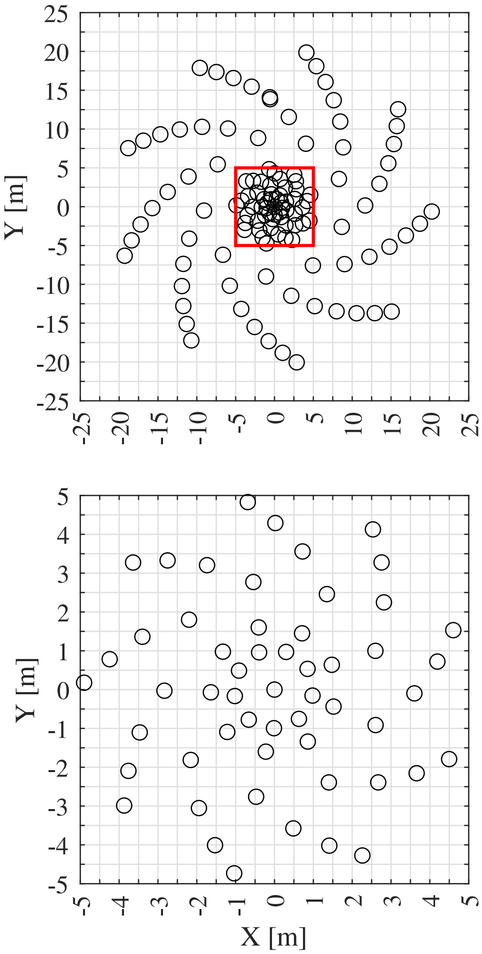

Figure 6: Day 201 phased array shown in local coordinate system. Top shows entire array with a red rectangle indicating the extents of the bottom figure, which shows the inner array more clearly.

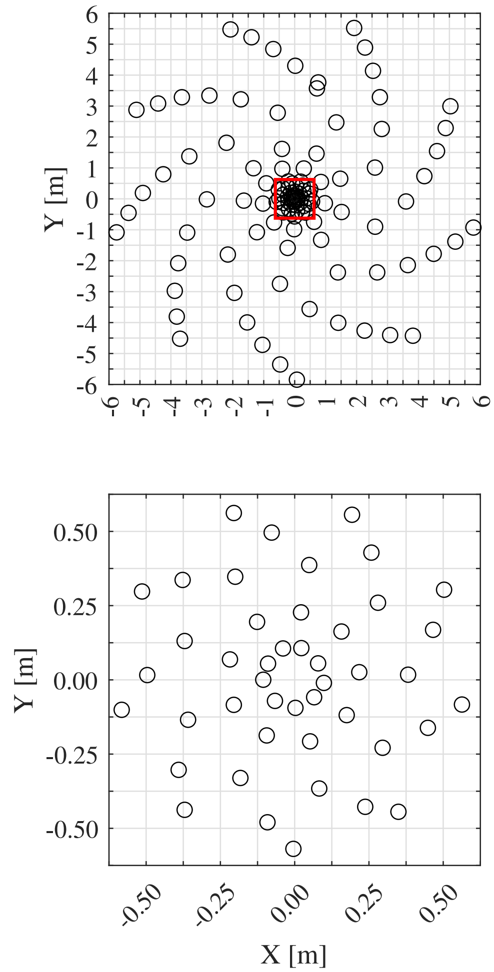

Figure 7: Day 209 phased array shown in local coordinate system. Top shows entire array with a red rectangle indicating the extents of the bottom figure, which shows the inner array more clearly.

low coherence across the microphone array. This necessitated a rapid reassessment and redesign of the phased array. The final phased array deployed also consisted of 117 microphones, and similar layout, but had a significantly smaller aperture. Day 209's phased array is shown in Figure 7. with an image from the helicopter's viewpoint shown in Figure 8.

The final nested design consists of an inner and an outer array to enable a broad working frequency range. Both subarrays were the result of an optimization to minimize the 3-dB beamwidth while maintaining peak sidelobes 10 dB down from the main lobe. The outer array is intended to cover 250 Hz to 1 kHz, while the inner array may be leveraged at 1 to 5 kHz. With a typical flight altitude of 61 m (200 ft), spatial resolution is lower than was desired but is the natural result of having to shrink the size of the phased array to account for the low coherence that was measured on the larger array (day 201's array). Significantly more details and analysis for this array are provided in Ref. 6.

Figure 8: Flight test image of day 209's phased array.

Weather Instrumentation

There was an extensive weather measurement capability deployed during this experiment. Two ZephIR 300 LiDARs were deployed, one near the snapshot array and another near the phased array. Each LiDAR is capable of measuring wind velocity at up to twelve programmable heights. The LiDAR deployed near the snapshot array was set to measure up to 300 m, at altitudes shown in Table 5. The phased array LiDAR, shown in Figure 9, measured up to 152 m; altitudes were chosen to measure the relevant portion of the atmosphere for flights over their specific array. Data from the LiDARs are sampled one altitude per second, and the results have been processed in 2 minute and 10 minute calibrated averages. There is at least one wind velocity profile measured within two minutes local to the microphone array for every test point.

Figure 9: LiDAR deployed near phased array.

A tethered weather balloon with weather sonde and temperature string, shown in Figure 10, was deployed throughout the test. The weather sonde on the balloon provides multiple measurements, including temperature, pressure, humidity, wind velocity, and altitude above ground level. The temperature string measures temperature approximately every 3 meters from ground level to sonde height. The weather balloon was deployed at the start of each test day to an altitude that reflected that day's objectives. Further, because the weather balloon was subject to winds and thermal changes, that altitude can be variable throughout a given day. All weather data have been post-processed such that each run has an associated weather sonde measurement at the current known altitude, as well as a temperature profile for the known altitude during that run.

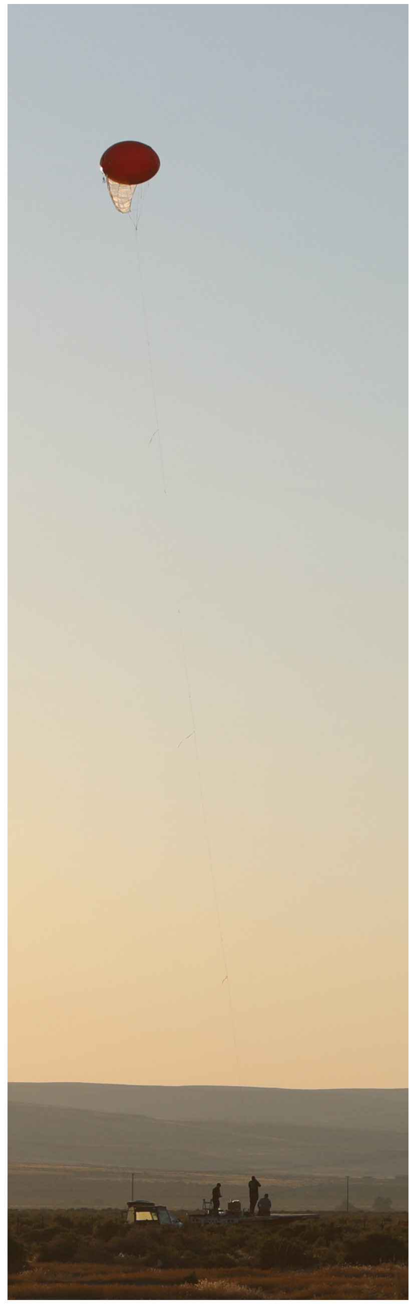

Figure 10: Tethered balloon with weather sonde and temperature string deployed near phased array.

Up to five ground-based weather stations were deployed around each array. These measured temperature, pressure, humidity, and wind velocity during each run. The weather stations were deployed at approximately two meters above ground level, and serve as a backup to the LiDAR and weather balloon systems.

Pilot Guidance

Two light systems were deployed to support guiding the pilot down the flight line and at the correct glideslope for each test condition. Runway end indicator lights (REIL) were repurposed and customized to include radio control, such that they flash down the center of the flight line to help the pilot stay on the correct azimuthal heading. Each REIL, one shown in Fig. 11, was also paired with a high-visibility tarp to help guide the pilot when the background light was too bright to pick out the REILs.

Figure 11: Runway end indicator light used for pilot azimuthal guidance down the flight path.

A four lamp precision approach path indicator system (PAPI) was also deployed during snapshot array days to assist the pilot in maintaining proper glideslope for that test condition. The PAPI system, previously described in Refs. 4, 12, is custom outfitted with linear actuators and is radio controlled from the MAF. Unlike traditional PAPIs, these can be adjusted to reflect the current required flight path angle (FPA) for pilot guidance, up to approximately 20° descent. The PAPI is only used for the snapshot array, as repositioning for the phased array would have delayed testing and limited data collection.

FLIGHT TEST CONDITIONS

The flight test conditions were split between snapshot and phased arrays, as each array targeted a different set of acoustic phenomena.

The pre-test designed constant airspeed snapshot flight test conditions are shown in Figure 12. Flight test conditions were assigned a prefix (‘L’ for level flight, ‘C’ for climb, and ‘D’ for descent) and numbered to identify each condition uniquely. Two full flight test days were dedicated to flights over the snapshot array. Each condition and the number of runs conducted at that condition over the snapshot array are provided

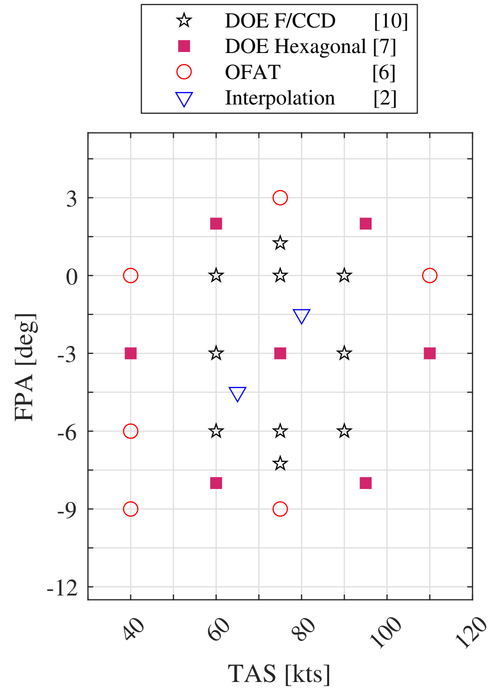

Figure 12: Dimensional conditions of all pre-test planned flight test runs for the snapshot array listed by true airspeed (TAS) and flight path angle (FPA).

in Table 6. All level flight conditions were flown at a target altitude of 61 m and through the center of the snapshot array. Hover conditions were performed over the center of the snapshot array at 61 m. Climb conditions were initiated at the edge of the snapshot array, from an altitude of 50 ft AGL. This ensured the vehicle was in a stable climb as it crossed the center of the array and not too high above ground level. Descent conditions started at least at the edge of the array, from an altitude that varied with flight path angle. Each descent condition had the same target location, the precision approach path indicators described above; thus the crossover altitude at the center of the snapshot array varied depending on flight path angle.

There was time to collect a target of opportunity data set, which focused on capturing transient maneuvering noise using the snapshot array. Eight test conditions were developed, all of which started from 75 knots in level flight at 61 m AGL. Those conditions and their counts are shown in Table 8. The maneuvers were initiated when the vehicle was in the center of the snapshot microphone array. The maneuvers were designed to primarily engage one pilot control at a time, and so speed and altitude could not be maintained throughout a maneuver. The pilot was instructed to terminate maneuvers such that they maintained a safe operating condition and to stay within the bounds of the vehicle limits. Regardless of instruction, the ‘fast’ maneuvers were particularly aggressive and proved to be invaluable data. A complete review of the maneuvering noise is provided in Ref. 8.

Design of Experiments

The snapshot array data included multiple different design of experiments (DOE) approaches. The standard one-factor-at-a-time (OFAT) approach was used, as well as several central composite designs and a hexagonal design. A face centered central composite design (FCD) was used and is depicted by the starred points shown in Fig. 12. The FCD includes test points on each corner of a cube, a test point in the center of each face, and a test point in the direct center of the cube. The FCD cube is defined from 60 to 90 knots, and 0 to -6° FPA.

A circumscribed central composite design (CCD) was also used, which includes similar test points as the FCD, but the test points on the center of each face are instead extended in the face-normal direction and are located on the surface of a sphere that circumscribes the test cube. This resulted in the additional starred points located at [75, 1.25°] and [75, -7.25°]. Additional points at [55, -3°] and [95, -3°] were neglected, as they would not likely be statistically different than the FCD points located only 5 knots away at [60, -3°] and [90, -3°], respectively.

A hexagonal approach was also used, which maintains three unique flight path angles similar to how the central composite designs are developed, but has five unique levels available in velocity. This design, represented by the filled squares in Fig. 12, does not extend to multidimensional space but allows for a greater extent of the flight envelope to be covered.

Those three DOE approaches together cover a significant portion of a traditional one-factor-at-a-time test campaign. Thus, the rest of the space is filled out with OFAT related test points, depicted by the circles in Fig. 12. Two additional points were necessary, however, to complete the evaluation. The purpose of DOE implementation is to enhance test efficiency, and so a response surface modeling (RSM) methodology was used. In order to test the accuracy of the RSM, it must be checked against extrapolation data points and interpolation data points. The OFAT test conditions serve as adequate extrapolation points for all DOE designs, but no interpolation points were available interior to the central composite designs. Thus, two additional interpolation points were chosen and are distinguished by the upside-down triangles in Fig. 12. More complete analysis of the DOE approach can be found in Ref. 7.

The DOE approach also resulted in the identification of additional test points. This was done by investigating the response surface models built from all microphones and determining their maximum values (M) or maximum derivative values (D) as predicted by the RSMs. Since there was additional time, points to match the phased array were also taken (P). The development of the new test conditions for the RSMs is discussed in full in Ref. 7. These new conditions are provided in Table 7.

Phased Array

The originally designed phased array test conditions are shown in Figure 13. The phased array test points, consisting only of constant airspeed conditions, were chosen using the traditional OFAT and focused on slower speeds, where the vehicle would spend more time over the array, due to directionality constraints of the phased array. Some points were chosen to overlap with snapshot array conditions shown in Fig. 12 for future comparison.

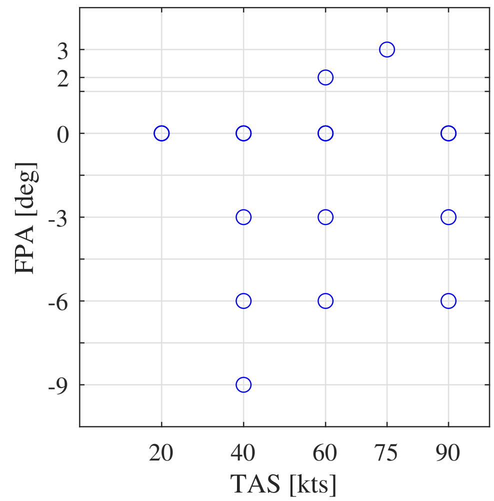

Figure 13: Dimensional conditions of all originally planned flight test runs for the phased array listed by true airspeed and flight path angle.

Phased array flight conditions follow a similar nomenclature as above, except 'P' is used as a prefix for clarity. Table 9 provides a list of the designed test conditions and the number of runs measured at each condition over day 201's phased array. Day 209's phased array flight conditions are found in Table 10.

Level flight conditions over the phased array were primarily tested at 61 m, but some conditions were conducted at 30 and 91 m to assess source map spatial resolution requirements. Phased array hover conditions 4, 5, and 6 are repeat conditions of 1, 2, and 3, respectively, but are held 46 m offset from the center of the array to investigate sideline capability. All climb and descent conditions for the phased array were initiated such that the crossover altitude was approximately 61 m.

Note, the number of runs provided in Tables 6-10 are the maximum number of repeats over each individual array. Due to multiple conditions, including but not limited to timing errors or inaccurate piloting, not all runs are viable for analysis.

RESULTS

Three acoustic test points will be investigated here, as a sample of the type of data that is available from this flight test.

These data will focus on a ‘L4’ – 90 knot level flight condition over the snapshot array, a ‘PL1’ – 20 knot level flight over the phased array, and an ‘M1’ – fast cyclic roll right maneuver noise condition over the snapshot array.

Weather Results

The weather for this flight test was remarkably good. Winds were exceptionally low, and temperatures and humidity (‘RH’) were as expected. Low humidity conditions (less than 20%) were experienced in the afternoon that can be problematic for atmospheric attenuation calculations. Data from ground-level weather stations around the microphone arrays, for the previously described conditions, can be found in Table 11. Unfortunately, the weather stations at the phased array blew over and broke prior to testing on the 209 array. So for those conditions, there are no ground based weather data and the meteorologic sensor on the LiDAR that was close to the phased array was used.

The wind speed gradient and temperature gradient for each of these conditions are shown in Figure 14. It can be seen that the winds were very low for this experiment and temperature gradients were not too large. There is a slight temperature inversion for the ‘L4’ and ‘PL1’ conditions, but the proximity of the aircraft to the snapshot array and phased array during measurements should negate any severe adverse impacts. Note, for the phased array day, only data from the LiDAR closest to the array is important. The other subfigures show both LiDARs and how consistent the winds were across the flight test area. Recall, the LiDAR near the phased array was set to scan lower altitudes than the snapshot array due to the flights occurring at a lower and closer proximity to the phased array than the snapshot array flights.

Aircraft Data Results

The instrumentation on-board the MD530F test vehicle, while extensive, did suffer some attrition prior to and throughout the test. Due to the complexity of the system – and an unfortunate mistake by hanger staff prior to the flight test – there were significant system failures. The system was repaired throughout the flight test, and some additional sensors broke during testing. All correctly measured data will be available in the future, but the test team is still combing through, identifying, and removing bad channels from the distribution data set.

Samples from measured sensors are provided for each of the three conditions under investigation. Figure 15 provides data from the ‘L4’ steady level flight condition. It can be seen that the roll, pitch, and flight path angles throughout the flight across the snapshot array are steady and near zero as expected. The pilot controls are also shown for each of the pilot’s inputs. Here, collective down, left pedal, right cyclic, and aft cyclic are all zero percent with 100% representing full travel in the opposite direction. The pilot controls indicate that this was a very stable flight condition.

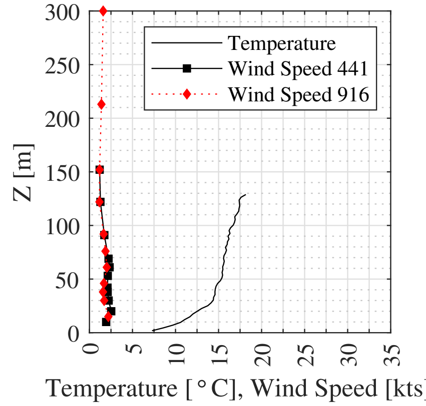

(a) L4

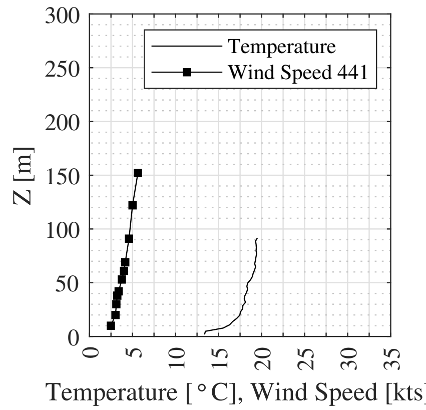

(b) PL1

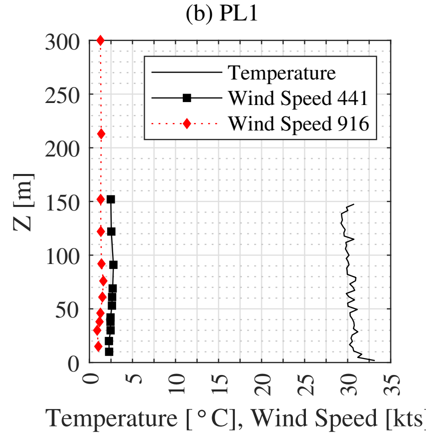

(c) M1

Figure 14: Wind speed and temperature profiles for (a) ‘L4’ sample test condition, (b) ‘PL1’ sample test condition, and (c) ‘M1’ sample test condition.

The shaft torque is shown in Fig. 15b, and some high frequency anomalies are present in the signal that should be filtered out prior to use in modeling. Overall, the shaft torque (measured below the rotor plane) is approximately 2500 ft-lbf, which combined with the constant 473 RPM (shown in

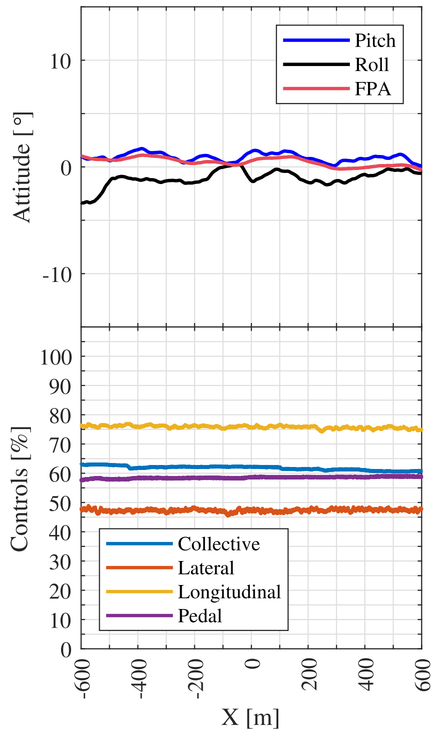

(a)

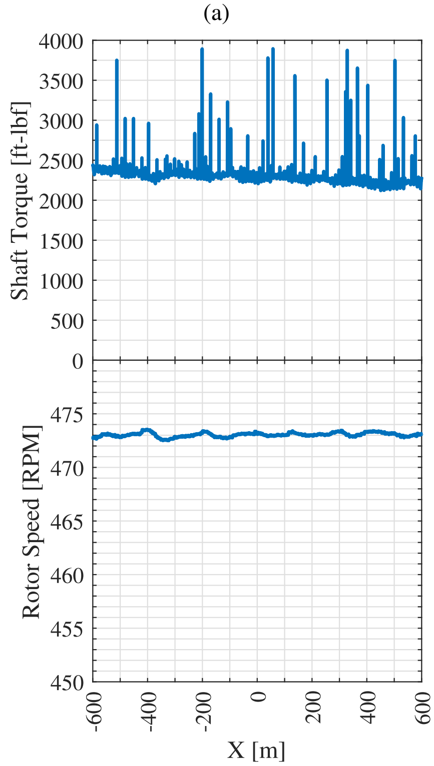

(b)

Figure 15: Sample aircraft sensor data measured during the 'L4' flight condition. (a) Shows the vehicle attitudes and pilot control positions, while (b) shows shaft torque and main rotor revolution rate.

Fig. 15b) results in approximately 207 horsepower to the rotor system for this condition.

Sample aircraft data for the 'PL1' condition are shown in Fig. 16. Note for this figure that the range of distance down the flight path is significantly reduced, compared to Fig. 15. This flight is over the phased array and only the portion of the data that is useful for phased array processing is presented. Comparing the two conditions, it can be seen that the pilot pulled more collective for this condition compared to the previous, but had smaller stick inputs.

There is an increased vehicle pitch noticed in Fig. 16a, compared to Fig. 15a, and that is because of the significant speed difference between the two conditions. The shaft torque sensor for this condition is improved as it is from later in the test, and the main rotor rotation rate shows the condition was flown close to 475 RPM resulting in a shaft horsepower of approximately 230.

By the time this condition was flown, the strain gauges on the pitch rod, longitudinal rod, collective rod, and damper were all repaired. These measurements are shown in Figure 17. The link loads show variation across the rotor revolutions, as expected.

The 'M1' fast cyclic roll right maneuver aircraft data are shown in Figure 18. This figure is useful but slightly less informative than the others. Each of the plots shown in this section is a function of flight path in the primary direction. Because the pilot turned to the right and started flying in the 'Y' direction, some of those data overlap themselves in the 'X' direction plots shown here. However, it can be seen that the pilot rapidly reached a 72 degree roll angle almost perfectly centered over the middle of the snapshot array. The collective controls read above 100%, which requires further analysis, but the other controls show the pilot attempted only to use the lateral cyclic to execute this mission, per instructions. This condition also had exceptional variation in main rotor rotation rate and shaft torque throughout the maneuver. The 'M1' condition is shown in significantly more detail in Ref. 8.

Acoustic Results

Acoustic emission data from the flight test can be investigated in many ways. A few samples are presented here based on previously described flight conditions. First, an investigation of the pressure time histories is conducted using a Vold-Kalman filter.

The second-generation Vold-Kalman filter (Ref. 17) can be utilized to extract and separate harmonic (i.e., shaft-coherent) content from the main and tail rotors from the overall pressure time history. Previous work has proven this order-tracking method to be effective for processing rotorcraft (Ref. 18) and UAM (Ref. 19) acoustic flight test data. Ultimately, the procedure enables greater physical insight into the snapshot hemi-

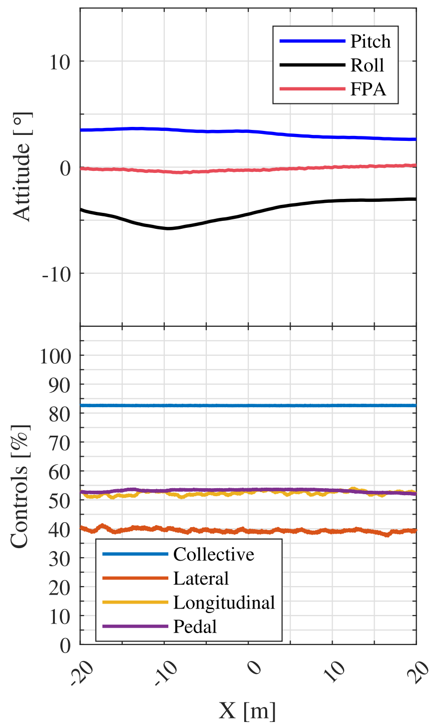

(a)

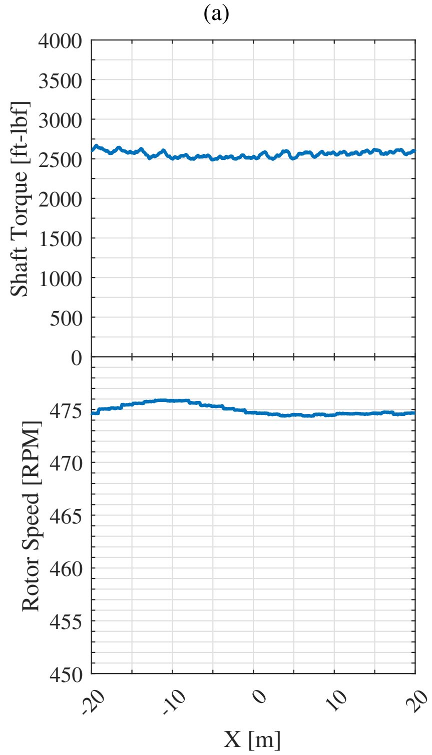

(b)

Figure 16: Sample aircraft sensor data measured during the 'PL1' flight condition. (a) Shows the vehicle attitudes and pilot control positions, while (b) shows shaft torque and main rotor revolution rate.

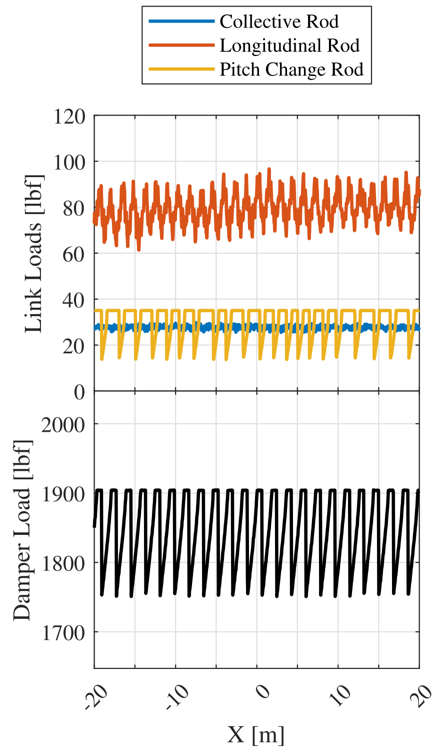

Figure 17: Measured link rod loads for 'PL1' maneuver of interest.

sphere data, particularly to extract waveforms and assess directivity variation of each rotor independently.

To implement, each individual acoustic signal is first de-Dopplerized using a time-domain formulation (Ref. 20) that leverages aircraft tracking data, synchronized with the acoustic signals, and microphone coordinates. The measured rotation rate of the main rotor is then used as an input to the Vold-Kalman filter to build the time-varying complex phasors intended to track the desired harmonic orders. The tail rotor gear ratio enables determination of the tail rotor phasors from the main rotor rotation rate. Selected orders for extraction include blade passage frequencies below 1 kHz for both rotors.

In this work, a single pole filter is implemented. Filter bandwidth was optimized for each individual harmonic order and acoustic signal. Optimization was accomplished by minimizing the difference in sound pressure level between a median-moving average of the original signal's spectra, to estimate the broadband shelf, and the autospectra of the residual (which is the time domain difference between the original signal and the harmonic content). This process resulted in bandwidths between 0.3 and 25 Hz. Harmonic signal reconstruction is then a superposition of the order waveforms.

A sample of the acoustic data for an 'L4' condition is shown in Fig. 19. This figure contains multiple subplots. The central image is a Lambert projection of the overall sound pressure level for the 90 knot level flight case. OASPL here is calculated from 10 Hz to 5 kHz, as no significant energy is

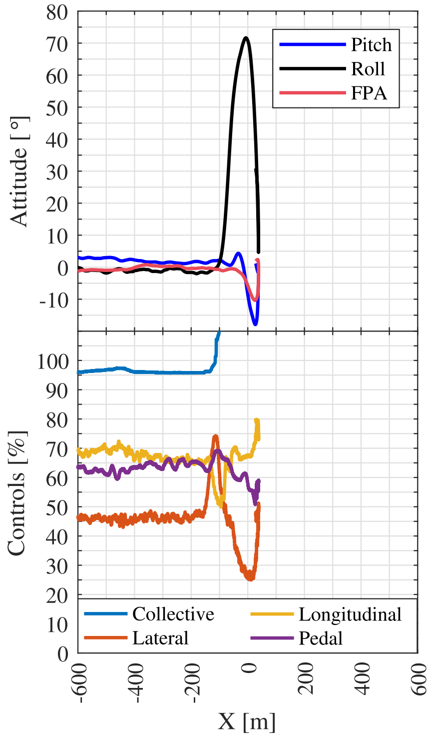

(a)

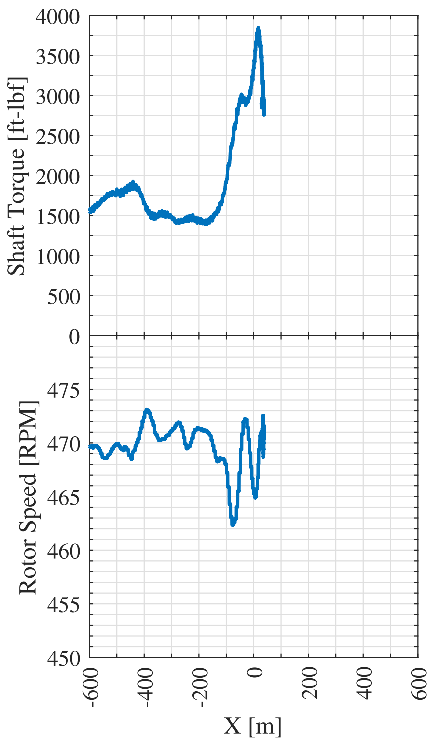

(b)

Figure 18: Sample aircraft sensor data measured during the ‘M1’ flight condition. (a) Shows the vehicle attitudes and pilot control positions, while (b) shows shaft torque and main rotor revolution rate.

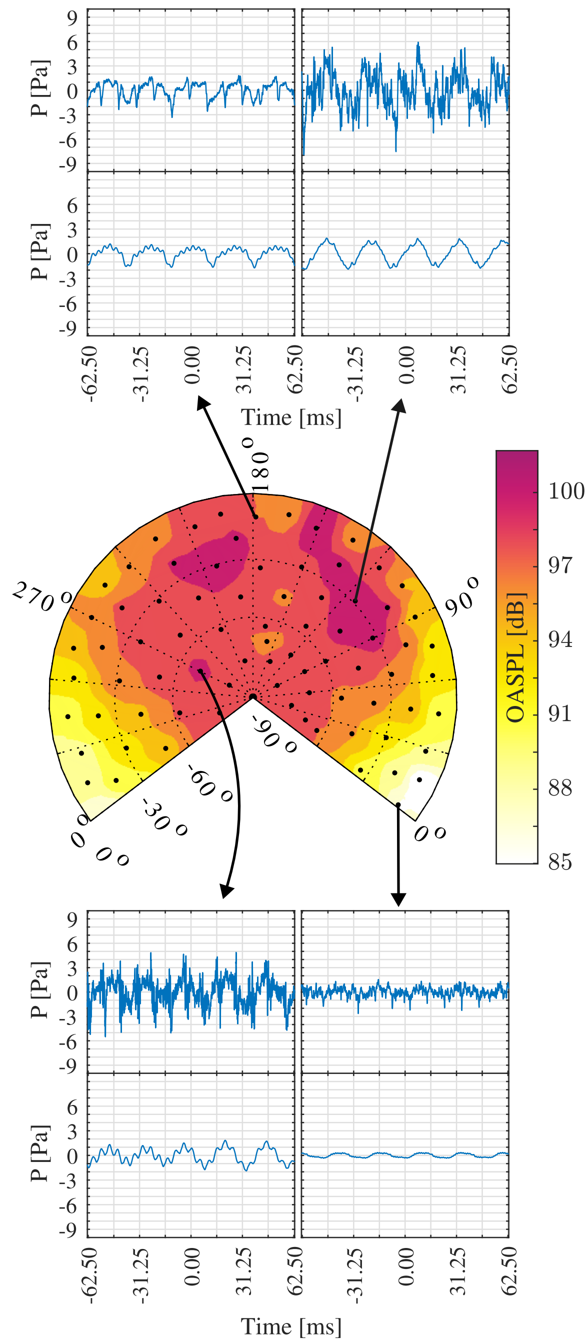

Figure 19: Composite image of acoustic emissions during an ‘L4’ condition. Center is a Lambert projection of OASPL measured by the snapshot array at the time of overpass. Surrounding are pressure time histories from sample microphones. The top of each time history is a quarter-second of unfiltered data centered on overpass, while the bottom is Vold-Kalman filtered main rotor signal for that same time period.

above that threshold. The surrounding figures are pressure time histories measured by the microphone indicated. Each subplot shows (top) the de-Dopplerized pressure time history and (bottom) main rotor extracted time history. Figure 20 shows the extracted hemisphere for the main rotor harmonics

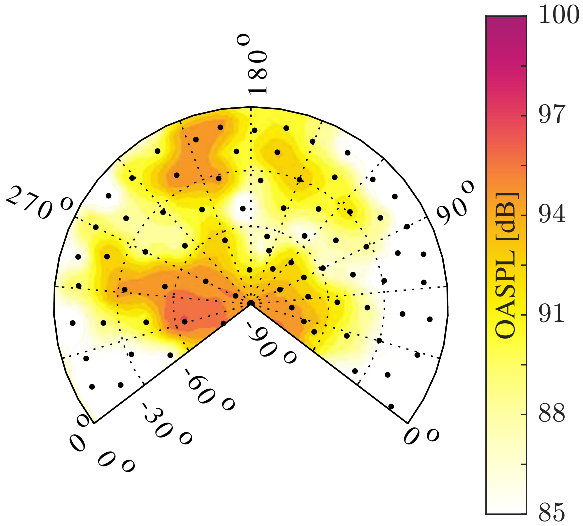

Figure 20: Main rotor extracted hemisphere OASPL for the 90 knot level flight case shown in Fig. 19.

below 1 kHz. Comparing Fig. 20 to Fig. 19, it is clear that the tail rotor and non-harmonic noises dominate the hemisphere in question.

The phased array data can similarly be synchronized with the main rotor rotation rate and used to analyze various source mechanisms on the aircraft. Figure 21 provides a sample im-

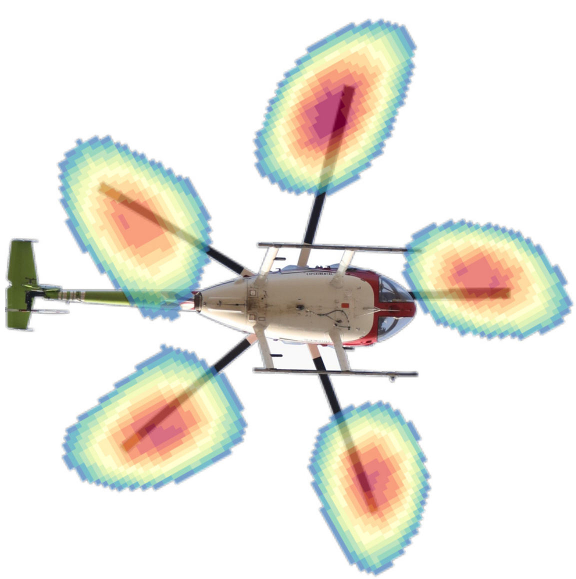

Figure 21: Phased array sample using ROSI derotational beamform method for the one-third octave band centered on 4 kHz. Flight condition is 'PL1' using Day 209's phased array.

age of a 4 kHz noise map produced by the 20 knot level flight condition ('PL1'). These data were processed using a ROtating Source Identifier method (ROSI) as developed in Ref. 21. From this image it is clear that the phased array deployed on day 209 is capable of distinguishing between each individual blade and provides useful information on noise source locations. Complete details of this method and other results from this flight test are provided in Ref. 6.

The final condition is the fast cyclic roll right condition. This highly transient acoustic maneuver condition cannot be adequately represented in a single sample acoustic image. Figure 22 shows the flight path of the maneuver as well as a single OASPL contour of the recorded signal. The OASPL shown in this image has been de-Dopplerized and distance corrected to 31 m radius from the vehicle, but is shown on the ground plane because the orientation of the vehicle results in a complicated semisphere of data. The OASPL has also been normalized, such that '0 dB' is the loudest OASPL value measured in a 75 knot level flight condition, the prescribed speed for this maneuver. The dashed line on Fig. 22b shows the 0 dB contour line, and it is clear that the majority of this condition is louder than the steady level flight equivalent. Ref. 8 provides analysis of this condition, along with other maneuver noise conditions.

CONCLUSIONS

A substantial acoustic flight test was documented. A fully instrumented MD530F vehicle was characterized using snapshot and phased microphone arrays. Sample figures were provided showing acoustic analysis for steady level flight and a transient maneuvering noise configuration. Analysis from each of the microphone arrays was provided, along with a full description of test conditions, on-board aircraft data, and weather system descriptions. The vast majority of the data presented here will be available to the public, with some data withheld due to the proprietary nature of the information. Once the on-board data reduction is complete, and the broken channels have been removed, a NASA technical memorandum fully documenting the test will be published and the data will be available at that time. There are multiple companion papers (Refs. 5–8) that more fully document the results of this experiment.

ACKNOWLEDGMENTS

The extensive nature of this flight test meant that a significant number of personnel were involved in making it a success. The following people were instrumental in ensuring this test was executed with exceptional precision, and cannot be thanked adequately. Helicopter Technology Company: Jay Wigginton (pilot extraordinaire), Charles 'Chuck' Dean (chief engineer and data system wizard), Jack Rajcic, Gary Budorf, Brian Cicerone. DEVCOM AvMC: Oliver Wong, Shawn Naigle, Tom Maier, Jacob Wilson. NASA LaRC:

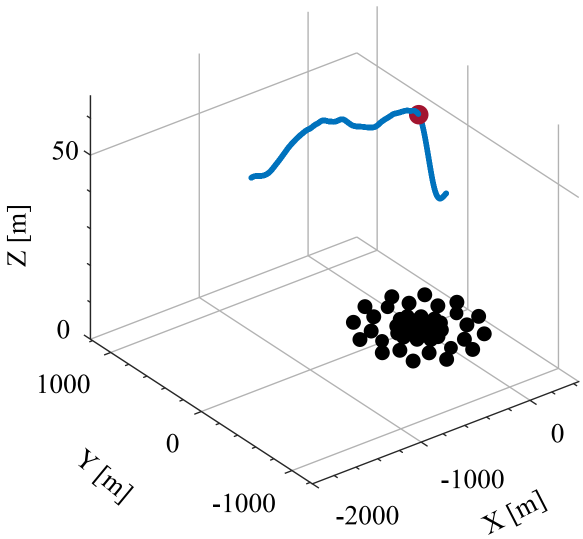

(a)

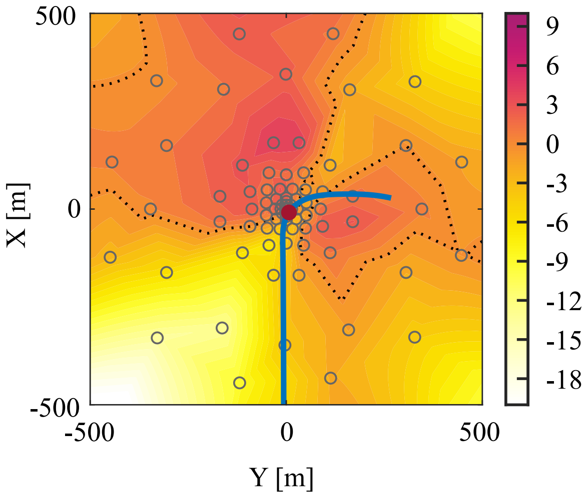

(b)

Figure 22: Flight path of maneuver relative to microphone locations is shown in (a), where the flight path is the blue line and the vehicle is located by the red circle at the instant under investigation. (b) Shows the OASPL on the ground plane that has been distance corrected to a sphere of constant radius, and the '0' dB mark indicates the loudest OASPL measured for a similar speed level flight condition.

Noah Schiller, Benny Lunsford, Michael Doty, Stanley Mason, Alonzo 'Max' Reid, Nikolas Zawodny, Tony Humphreys, Nathan Cruze, and Peter A. Parker. Analytical Mechanics Associates: Jeffrey Davis and David Ridgway. Sierra Army Depot: Margarita Gonzalez-Venegas, Michael Foley, and Michael Gray.

REFERENCES

1. Lin II, R.-G., "L.A. County backs federal restriction of low-flying helicopters," *LA Times*, Available at: `http://latimesblogs.latimes.com/lanow/2011/11/la-county-backs-restriction-of-low-flying-helicopters.html` (Accessed: 1 April 2021), November 2011.

2. Anderson, N., "Chesapeake to purchase 162 acres of land for buffer between naval airport, homes," *The Virginian-Pilot*, Available at: `https://www.pilotonline.com/2022/10/03/chesapeake-to-purchase-162-acres-of-land-for-buffer-between-naval-airport-homes` (Accessed: 28 Jan 2025), 2022.

3. Allen-Ebrahimian, B., ""Osprey get out:" Okinawa protesters call for closure of U.S. military bases," *AXIOS*, Available at: `https://www.axios.com/2023/05/13/okinawa-protests-us-military-bases-close` (Accessed: 28 Jan 2025), May 2023.

4. Stephenson, J. H., Lind, A., Hutchins, C., Pascioni, K., Houston, M. L., and Martin, P., "Yuma 2022 Rotorcraft Acoustic Flight Test," Technical Memorandum NASA/TM-20220004483, NASA Langley Research Center, Hampton, VA 23681, USA, April 2022.

5. Houston, M. L., Stephenson, J. H., Pascioni, K. A., and Stutz, C. M., "Snapshot Array Design Considerations for Rotorcraft Noise Characterization," Proceedings of the 81st Annual Forum of the Vertical Flight Society, Virginia Beach, VA, May 2025.

6. Pascioni, K. A., Stutz, C. M., Houston, M. L., and Stephenson, J. H., "Phased Array Measurements on a Full-Scale Helicopter," Proceedings of the 81st Annual Forum of the Vertical Flight Society, Virginia Beach, VA, May 2025.

7. Stephenson, J. H. and Pascioni, K. A., "Design of Experiments Development for Rotorcraft Acoustic Flight Testing," Proceedings of the 81st Annual Forum of the Vertical Flight Society, Virginia Beach, VA, May 2025.

8. Stutz, C. M., Stephenson, J. H., Pascioni, K. A., and Houston, M. L., "Acoustic Assessment of an MD530F Helicopter in Maneuvering Flight," Proceedings of the 81st Annual Forum of the Vertical Flight Society, Virginia Beach, VA, May 2025.

9. "N20AT FAA Registry Information," Technical report, Federal Aviation Authority, Available at: `https://registry.faa.gov/AircraftInquiry/Search/NNumberResult?nNumberTxt=20AT`, Accessed 30 Jan 2025.

10. Pascioni, K. A., Stephenson, J. H., Houston, M. L., and Stutz, C. M., "Overview of the 2024 Army/NASA

Acoustic Research Flight Test," NASA Acoustics Technical Working Group Meeting, Fall 2024, Cleveland, Ohio, October 2024.

11. Webre, J. L., White, M., Stormer, W., Abbott, W., and Gould, W., "Airworthiness and flight characteristics evaluation of the McDonnell Douglas Helicopter Corporation (MDHC) 530FF helicopter," Final Report, AD-A218 253, Aviation Engineering Flight Activity, Edwards Air Force Base, CA, 93523-5000 USA, May 1989.

12. Pascioni, K. A., Greenwood, E., Watts, M. E., Smith, C. D., and Stephenson, J. H., "Medium-Sized Helicopter Noise Abatement Flight Test Data Report," Technical Memorandum TM-20210011459, NASA Langley Research Center, Hampton, VA 23681, USA, July 2021.

13. "Ground-Plane Microphone Configuration for Propeller-Driven Light-Aircraft Noise Measurement," ARP 4055, SAE, November 2007.

14. Humphreys Jr, W. M., Lockard, D. P., Khorrami, M. R., Culliton, W. G., McSwain, R. G., Dolph, C. V., and Ravetta, P. A., "Development of a Field-Deployable Microphone Phased Array for Airframe Noise Flyover Measurements," Technical Memorandum TM-20230010620, NASA Langley Research Center, Hampton, VA 23681, USA, August 2023.

15. Page, J. A., Wilmer, C., Schultz, T., Plotkin, K. J., and Czech, J., "Advanced Acoustic Model Technical Reference and User Manual," Technical Report Project WP-1304, SERDP, May 2009.

16. Lebedev, V. and Laikov, D., "A Quadrature Formula for the Sphere of the 131$^{\text{st}}$ Algebraic Order of Accuracy," *Doklady Mathematics*, Vol. 59, (3), 1999, pp. 477–481.

17. Vold, H. and Leuridan, J., "High Resolution Order Tracking at Extreme Slew Rates using Kalman Tracking Filters," SAE Technical Paper 931288, 1993.

18. Rachaprolu, J. and Greenwood, E., "Helicopter noise source separation using an order tracking filter," *Journal of the American Helicopter Society*, Vol. 69, (012006), 2024.

19. Pascioni, K. A., Thai, A. D., and Bain, J. J., "Propeller Source Noise Separation from Flight Test Measurements of the Joby Aviation Aircraft," 30th AIAA/CEAS Aeroacoustics Conference, Rome, Italy, June 2024.

20. Greenwood, E. and Schmitz, F. H., "Separation of Main and Tail Rotor Noise from Ground-Based Acoustic Measurements," *Journal of Aircraft*, Vol. 51, (2), March 2014, pp. 464–472.

21. Sijtsma, P., Oerlemans, S., and Holthusen, H., "Location of rotating sources by phased array measurements," 7th AIAA/CEAS Aeroacoustics Conference and Exhibit, 2001.

Table 1: Aircraft rotor specifications extracted from Ref. 11.

No. Main Rotor Blades	5
Main Rotor Diameter	8.34 m
Main Rotor RPM; BPF	477; 39.75 Hz
Main Rotor Blade Chord (constant)	17.15 cm
Main Rotor Blade Twist	9.5°
Main Rotor δ_3	0°
Main Rotor Flap Hinge Offset	15.24 cm
No. Tail Rotor Blades	2
Tail Rotor Diameter	1.45 m
Tail Rotor RPM; BPF	2,848; 94.9 Hz
Tail Rotor Blade Chord (constant)	13.54 cm
Tail Rotor Blade Twist	9.5°
Tail Rotor δ_3	30°
Empty Weight	782 kg

Table 2: Processed MD530 vehicle state data variables from ANTS.

Variable Name	Description	Units
Time	UTC seconds after midnight	seconds
Heading	Current vehicle heading relative to magnetic North	$^\circ$
GPSX	Vehicle position in ‘X’	m
GPSY	Vehicle position in ‘Y’	m
GPSZ	Vehicle position in ‘Z’	m
GroundSpdX	Vehicle speed in ‘X’ direction	kts
GroundSpdY	Vehicle speed in ‘Y’ direction	kts
GroundSpdZ	Vehicle speed in ‘Z’ direction	kts
GroundSpdKts	Total vehicle speed in ‘X’ and ‘Y’ direction	kts
AccelX	Vehicle acceleration in ‘X’ direction	g’s
AccelY	Vehicle acceleration in ‘Y’ direction	g’s
AccelZ	Vehicle acceleration in ‘Z’ direction	g’s
AccelGrSpd	Total vehicle acceleration in ‘X and ‘Y’ direction	g’s
AccelG	Total vehicle acceleration in ‘X, ‘Y’, and ‘Z’ direction	g’s
Pitch	Vehicle pitch	$^\circ$
Roll	Vehicle roll	$^\circ$
FPA	Flight path angle	$^\circ$

Table 3: MD530F on board data variables, including units and sampling rates.

Description	Variable Name	Units	Sampling Rate [Hz]
Main rotor rotation rate	ROTOR_RPM	RPM	128
Longitudinal mast bending at waterline station 68.25	MASTLONUPR_68_25	in-lbf	128
Lateral mast bending at waterline station 68.25	MASTLATUPR_68_25	in-lbf	128
Engine torque	ENGINE_TORQUE	ft-lbf	128
Throttle control position	THROTPOS	%	128
Longitudinal link axial load	LOADLINK	lbf	256
Collective control rod axial load	COLLROD	lbf	256
Longitudinal mast bending at waterline station 73.0	MASTLONUPR_73	in-lbf	256
Lateral mast bending at waterline station 73.0	MASTLATUPR_73	in-lbf	256
Longitudinal cyclic stick control position	LONCONPOS	%	256
Lateral cyclic stick control position	LATCONPOS	%	256
Pedal position (directional control)	DIRCONPOS	%	256
Collective control position	COLLCONPOS	%	256
Pitch change link axial load	PCLINK	lbf	256
Damper rod axial load	DAMPER	lbf	256
Drive shaft torsion	SHAFTTOR1	in-lbf	256
Tail boom torsion at waterline station 258	TBTOR258	in-lbf	256
Tail boom torsion at waterline station 211	TBTOR211	in-lbf	256
Vertical stabilizer middle	VERTMID	in-lbf	256
Vertical stabilizer upper	VERTUP	in-lbf	256
Horizontal stabilizer bending fwd & right	HZFWDRH	in-lbf	256
Horizontal stabilizer bending aft & right	HZAFTRH	in-lbf	256
Horizontal stabilizer bending fwd & left	HZFWDLH	in-lbf	256
Horizontal stabilizer bending aft & left	HZAFTLH	in-lbf	256
Tail boom vertical bending at waterline station 211	TBVERT211	in-lbf	512
Tail boom vertical bending at waterline station 258	TBVERT258	in-lbf	512
Tail boom lateral bending at waterline station 211	TBLAT211	in-lbf	512
Tail boom lateral bending at waterline station 258	TBLAT258	in-lbf	512
Rotor azimuth channel 1	ROTOR_AZ1	volts	512
Rotor azimuth channel 2	ROTOR_AZ2	volts	512

Table 4: Tabulated microphone numbers and locations for snapshot array.

Mic #	'X' [m]	'Y' [m]	'Z' [m]	Azimuth [°]	Elevation [°]	Mic #	'X' [m]	'Y' [m]	'Z' [m]	Azimuth [°]	Elevation [°]
1	447.5	119.8	-0.1	195.0	-7.5	41	-44.1	92.5	-0.2	295.5	-30.8
2	327.9	330.7	-0.3	225.2	-7.5	42	-92.4	44.1	-0.1	334.5	-30.8
3	120.1	444.4	-0.5	254.9	-7.6	43	-87.4	-0.1	-0.2	0.1	-35.0
4	-123.1	449.0	-0.5	285.3	-7.5	44	-92.4	-44.3	-0.1	25.6	-30.8
5	-329.1	328.9	-0.3	315.0	-7.5	45	-44.1	-92.7	-0.3	64.6	-30.8
6	-444.0	118.9	-0.4	345.0	-7.6	46	0.1	-87.6	-0.1	90.1	-34.9
7	-432.0	-113.2	-0.2	14.7	-7.8	47	44.4	-92.6	-0.2	115.6	-30.8
8	-327.4	-327.6	-0.4	45.0	-7.5	48	92.8	-44.3	-0.2	154.5	-30.7
9	-118.3	-446.5	-0.2	75.2	-7.5	49	51.0	15.8	-0.2	197.2	-48.8
10	120.0	-447.4	-0.2	105.0	-7.5	50	49.2	48.9	-0.2	224.9	-41.4
11	325.5	-328.4	-0.1	134.8	-7.5	51	16.1	50.8	-0.2	252.4	-48.9
12	448.0	-119.5	-0.2	165.1	-7.5	52	-15.8	50.8	-0.2	287.3	-49.0
13	345.2	-0.8	-0.2	179.9	-10.0	53	-48.8	48.9	-0.1	315.0	-41.5
14	306.0	159.8	-0.2	207.6	-10.0	54	-50.7	15.8	-0.2	342.7	-49.0
15	162.3	305.3	-0.3	242.0	-10.0	55	-50.8	-16.0	-0.1	17.5	-48.9
16	0.1	345.7	-0.3	270.0	-10.0	56	-48.8	-49.1	-0.2	45.1	-41.4
17	-162.0	305.3	-0.3	298.0	-10.1	57	-15.8	-51.0	-0.1	72.8	-48.9
18	-303.8	163.5	-0.1	331.7	-10.0	58	16.1	-51.0	-0.2	107.5	-48.8
19	-345.6	-0.1	-0.2	0.0	-10.0	59	49.1	-49.1	-0.2	135.0	-41.4
20	-308.7	-159.1	-0.2	27.3	-10.0	60	51.1	-16.0	-0.1	162.6	-48.8
21	-162.0	-305.5	-0.2	62.1	-10.0	61	28.4	-0.1	-0.2	179.7	-65.1
22	0.2	-345.9	-0.2	90.0	-10.0	62	25.3	25.0	-0.2	224.7	-59.8
23	162.3	-305.5	-0.2	118.0	-10.0	63	0.1	28.2	-0.0	269.7	-65.2
24	304.9	-161.8	-0.3	152.0	-10.1	64	-25.0	25.0	-0.2	314.9	-59.9
25	169.4	32.4	-0.1	190.8	-19.5	65	-28.1	-0.1	-0.2	0.3	-65.3
26	111.9	111.7	-0.2	224.9	-21.1	66	-25.0	-25.2	-0.2	45.3	-59.9
27	32.6	169.1	-0.2	259.1	-19.6	67	0.1	-28.3	-0.1	90.3	-65.1
28	-32.3	169.2	-0.1	280.8	-19.5	68	25.3	-25.3	-0.2	135.0	-59.7
29	-111.7	111.7	-0.1	315.0	-21.1	69	19.5	-0.1	-0.2	179.8	-72.3
30	-169.1	32.4	-0.1	349.2	-19.5	70	10.5	10.3	-0.2	224.3	-76.5
31	-169.1	-32.6	-0.2	10.9	-19.5	71	0.2	13.7	0.0	269.2	-77.4
32	-111.6	-111.9	-0.2	45.1	-21.1	72	-10.2	10.2	-0.2	315.1	-76.7
33	-32.3	-169.4	-0.1	79.2	-19.5	73	-19.1	-0.0	-0.1	0.1	-72.6
34	32.6	-169.4	-0.2	100.9	-19.5	74	-10.2	-10.4	-0.1	45.6	-76.6
35	112.0	-111.9	-0.2	135.0	-21.1	75	0.2	-13.8	-0.0	90.7	-77.3
36	169.4	-32.5	-0.1	169.1	-19.5	76	10.5	-10.4	-0.2	135.1	-76.4
37	87.7	-0.1	-0.2	179.9	-34.9	77	9.8	-0.2	-0.2	179.0	-80.9
38	92.8	44.1	-0.2	205.4	-30.8	78	-9.5	-0.1	-0.1	0.4	-81.2
39	44.4	92.4	-0.2	244.4	-30.8	79	0.0	0.0	0.0	180.0	-90.0
40	0.0	87.5	-0.0	270.0	-34.9						

Table 5: Prescribed LiDAR altitudes (in meters).

Snapshot Array LiDAR #916	Phased Array LiDAR #441
0	0
15	10
30	20
38	30
46	38
61	42
76	53
92	61
122	69
152	91
213	122
300	152

Table 6: Flight condition names, prescribed flight conditions, and number of measured runs at that condition.

Condition Code	TAS [kts]	FPA [°]	Runs
C1	75	3	5
C2	60	2	5
C3	95	2	5
C4	75	1	5
L1	40	0	4
L2	60	0	5
L3	75	0	5
L4	90	0	9
L5	110	0	4
D1	80	-1.5	3
D2	40	-3	5
D3	60	-3	5
D4	75	-3	5
D5	90	-3	5
D6	110	-3	5
D7	65	-4.5	3
D8	40	-6	3
D9	60	-6	5
D10	75	-6	5
D11	90	-6	5
D12	75	-7.25	5
D13	60	-8	5
D14	95	-8	6
D15	40	-9	3
D16	75	-9	3
H1	0	0	1
H2	0	0	1

Table 7: Flight condition names developed during the flight test, prescribed flight conditions, and number of measured runs at that condition. The final column indicates that the point was developed to match the phased array (P), based on the RSM models for maximum (M) metric and derivative (D) of the metric.

Condition Code	TAS [kts]	FPA [°]	Runs	Reason
C5	40	3	3	D
C6	60	3	3	D
C7	95	3	3	D
C8	40	5	3	D
C9	60	5	3	D
C10	75	5	3	M
C11	90	5	3	M
L6	20	0	3	P
D17	75	-10.5	5	P
D18	40	-12	3	D
D19	60	-12	3	M
D20	75	-12	4	D/M

Table 8: Maneuvering flight condition names, their description, and number of measured runs at that condition.

Condition Code	Description	Runs
M1	Cyclic roll right fast	2
M2	Cyclic roll right slow	2
M3	Cyclic roll left fast	2
M4	Cyclic roll left slow	2
M5	Cyclic pitch up fast	2
M6	Collective pitch up fast	2
M7	Collective + cyclic pitch up fast	2
M8	Push over fast	2

Table 9: Flight condition names, prescribed flight conditions, and number of measured runs at that condition for day 201's phased array.

Condition Code	TAS [kts]	FPA [°]	Crossover Altitude [m]	Runs
PC1	75	3	61	2
PC2	60	2	61	2
PL1	20	0	61	8
PL2	40	0	61	8
PL3	60	0	61	10
PL4	90	0	61	9
PL5	20	0	30	4
PL6	40	0	30	4
PL7	60	0	30	4
PL8	90	0	30	2
PL9	110	0	61	8
PD1	80	-2	61	3
PD2	40	-3	61	3
PD3	60	-3	61	3
PD4	75	-3	61	2
PD5	90	-3	61	2
PD6	110	-3	61	2
PD9	60	-6	61	2
PD10	75	-6	61	2
PD11	90	-6	61	2
PD13	60	-9	61	2
PD15	40	-9	61	2
PD16	75	-9	61	2
PD17	75	-10	61	2
PH1	0	0	61	7
PH2	0	0	91	6
PH3	0	0	122	3

Table 10: Flight condition names, prescribed flight conditions, and number of measured runs at that condition for day 209's phased array.

Condition Code	TAS [kts]	FPA [°]	Crossover Altitude [m]	Runs
PC1	75	3	61	2
PC2	60	2	61	2
PL1	20	0	61	4
PL2	40	0	61	4
PL3	60	0	61	5
PL4	90	0	61	4
PL5	20	0	30	2
PL6	40	0	30	2
PL7	60	0	30	2
PL8	90	0	30	2
PL9	110	0	61	2
PL11	40	0	91	2
PL12	60	0	91	2
PL13	90	0	91	2
PL14	110	0	91	2
PD1	80	-2	61	2
PD2	40	-3	61	2
PD3	60	-3	61	2
PD4	75	-3	61	2
PD5	90	-3	61	2
PD6	110	-3	61	2
PD9	60	-6	61	2
PD10	75	-6	61	2
PH1	0	0	61	4
PH2	0	0	91	3
PH3	0	0	122	2
PH4	0	0	61	2
PH5	0	0	91	2
PH6	0	0	122	2

Table 11: Ground based weather data for sample flight conditions. 'Mic. #' refers to the microphone location at which a weather station was placed, or refers specifically to which LiDAR the data came from.

Mic. #	Temp. [°C]	Press. [kPa]	RH [%]	Wind Spd. [kts]	Wind Dir. [°]
		'L4' Condition			
1	9.3	88.4	38	0	38
6	11.1	88.4	41	0	46
10	10.4	88.4	41	0	347
79	11.0	88.4	41	0	101
		'PL1' Condition			
LiDAR 441	12.9	87.2	45		
		'M1' Condition			
1	31.0	88.5	23	0	329
6	31.5	88.6	23	0	313
10	32.4	88.5	24	0	282
79	31.2	88.5	26	1	276